coatings

MDPI

Article

Sol-Gel Derived ZnO Thin Films with Nonvolatile Resistive Switching Behavior for Future Memory Applications

Xiangqian Shen [1,2] and Zhiqiang Yu [3,4,*]

[1] Xinjiang Key Laboratory of Solid State Physics and Devices, School of Physical Science and Technology, Xinjiang University, Urumqi 830046, China; sxqlyq@sjtu.edu.cn
[2] State Key Laboratory of Metal Matrix Composites, Shanghai Jiao Tong University, Shanghai 200240, China
[3] School of Electronic Engineering, Guangxi University of Science and Technology, Liuzhou 545006, China
[4] Wuhan National Laboratory for Optoelectronics, School of Optical and Electronic Information, Huazhong University of Science and Technology, Wuhan 430074, China
* Correspondence: zhiqiangyu@alumni.hust.edu.cn

Abstract: Herein we report on a facile sol-gel spin-coating technique to fabricate ZnO thin films that grow preferentially along the (002) plane on FTO substrates. By employing the magnetron sputtering technique to deposit a tungsten (W) top metal electrode onto these ZnO thin films, we successfully realize a W/ZnO/FTO memory device that exhibits self-rectifying and forming-free resistive switching characteristics. Notably, the as-prepared device demonstrates impressive non-volatile and bipolar resistive switching behavior, with a high resistance ratio (R_{HRS}/R_{LRS}) exceeding two orders of magnitude at a reading voltage of 0.1 V. Moreover, it exhibits ultralow set and reset voltages of approximately +0.5 V and −1 V, respectively, along with exceptional durability. In terms of carrier transport properties, the low resistance state of the device is dominated by ohmic conduction, whereas the high resistance state is characterized by trap-controlled space-charge-limited current conduction. This work highlights the potential of the ZnO-based W/ZnO/FTO memory device as a promising candidate for future high-density nonvolatile memory applications.

Keywords: self-rectifying; resistive switching; ZnO thin films; nonvolatile memory device; sol-gel spin-coating

check for updates

Citation: Shen, X.; Yu, Z. Sol-Gel Derived ZnO Thin Films with Nonvolatile Resistive Switching Behavior for Future Memory Applications. *Coatings* **2024**, *14*, 824. https://doi.org/10.3390/coatings14070824

Academic Editor: Olga A. Shilova

Received: 4 June 2024
Revised: 28 June 2024
Accepted: 29 June 2024
Published: 2 July 2024

Copyright: © 2024 by the authors. Licensee MDPI, Basel, Switzerland. This article is an open access article distributed under the terms and conditions of the Creative Commons Attribution (CC BY) license (https://creativecommons.org/licenses/by/4.0/).

1. Introduction

Resistive switching random access memory (ReRAM) has established itself as a frontier technology in the realm of nonvolatile memory devices [1–12]. Boasting an array of advantages including straightforward architecture, remarkable reliability, minimal power consumption, robust durability, ultra-compact stacking, and multistate resistive switching capabilities, ReRAM has found widespread application in various fields such as space technology, optoelectronics, mobile devices, the internet of things, and high-density data storage [13–25]. One of the key attributes that sets ReRAM apart is its electric field-induced resistive switching behavior, which enables non-volatile data storage with low operational voltage, non-destructive readout capabilities, rapid switching speeds, and promising scalability potential [26–30]. Resistive switching refers to the reversible change in the resistance state of a material in response to an impressed electric field or voltage [31–48]. In ReRAM devices, this phenomenon is exploited to store information in the form of high resistance state (HRS) and low resistance state (LRS) [49–56]. The HRS typically represents the "off" or erased state, while the LRS corresponds to the "on" or programmed state. The resistance ratio between these two states, denoted as R_{HRS}/R_{LRS}, serves as a critical parameter for evaluating ReRAM performance. This ratio essentially quantifies the difference in resistance between the HRS and LRS, representing the read margin. A higher resistance ratio translates to a larger read margin, ensuring a more reliable distinction between the two states during the read operation. With a large read margin,

the devices can confidently identify the stored information's state, whether it is "on" or "off", even in the presence of noise or fluctuations in operating conditions. This enhances the reliability and durability of ReRAM devices, positioning them as promising candidates for future storage technologies [57–63].

Transition metal oxides, including ZnO [3–7], TiO_2 [8–10,22,56,58–60], HfO_2 [11], GaO_x [12], α-Fe_2O_3 [13], Co_3O_4 [14], CuO_x [15,23], WO_3 [16], NiO [17], In_2O_3 [18], TaO_x [19], and CeO_2 [20], have garnered significant interest in nonvolatile memory devices due to their unique chemical and physical properties. These oxides exhibit variable resistance, enabling them to switch between high and low resistance states in response to an applied electric field. This resistive switching behavior allows them to store and retrieve information in a nonvolatile manner, meaning that the stored data persist even when the power supply is disconnected. Furthermore, transition metal oxides possess a high on/off ratio, enhancing the reliability of the memory device by reducing the chances of misreading stored information. Additionally, they demonstrate good endurance and retention, making them suitable for repeated usage over long periods of time. These characteristics, along with their scalability and compatibility with CMOS technology, position transition metal oxides as promising candidates for high-density, energy-efficient nonvolatile memory solutions. Among the materials mentioned above, ZnO has garnered particular attention. ZnO possesses a suitable energy gap of 3.37 eV, which enables efficient electronic transport. Additionally, its nontoxic nature and high exciton-binding energy of 60 meV contribute to its stability and reliability as a memory material. Furthermore, ZnO exhibits high electron mobility (~120 cm^2/Vs), which is essential for achieving fast switching speeds in ReRAM devices. In recent years, numerous ZnO nanomaterial-based ReRAMs have been developed and exhibited exceptional resistive switching capabilities [3–7,24–47]. However, there remains a dearth of reports documenting the unique self-rectifying and forming-free resistive switching behaviors demonstrated by these devices. Furthermore, the underlying mechanism accountable for these distinctive resistive switching behaviors remains elusive.

A diverse array of synthesis techniques has been utilized in the fabrication of ZnO nano-film-based memory devices [21,28,30,43,44,49,52,53]. Among them, direct current (DC) magnetron sputtering, spray pyrolysis, electron beam evaporation, and spin-coating are the most commonly used methods. Each of these techniques possesses distinct characteristics and offers its own set of advantages. DC magnetron sputtering involves the use of a magnetically confined plasma to sputter ZnO target material onto a substrate [25]. This method offers high deposition rates and good adhesion. It is suitable for large-scale production and can produce films with high purity and density. Spray pyrolysis is a chemical method that involves spraying a solution of ZnO precursors onto a heated substrate, resulting in the decomposition and deposition of ZnO [26]. This technique is cost-effective and suitable for depositing films on complex-shaped substrates. However, it may result in films with lower purity and density compared to other methods. Electron beam evaporation utilizes a focused electron beam to heat and evaporate ZnO material, which then condenses on the substrate to form a film [33]. This method offers high deposition rates and the ability to evaporate high-melting-point materials. The resulting films often have good uniformity and purity. On the other hand, spin-coating involves depositing a solution of ZnO precursors onto a rotating substrate, utilizing centrifugal force to form a uniform film [5,6,24,46]. This technique is simple, inexpensive, and particularly suitable for depositing thin films on small-sized substrates. Spin-coating also allows for precise control of film thickness, making it a highly versatile and practical method.

In this study, ZnO thin films preferentially grown along the (002) plane were fabricated via a sol-gel spin-coating method on an FTO substrate. The photoelectric and semiconductor properties of the resulting memory device consist of W/ZnO/FTO were thoroughly investigated. Notably, the device exhibited remarkable nonvolatile and bipolar resistive switching behavior, characterized by a significant resistance ratio (R_{HRS}/R_{LRS}) exceeding two orders of magnitude at a reading voltage of 0.1 V. Furthermore, it demonstrated highly repeatable and reliable switching behaviors and ultralow set and reset voltages, as well as

exceptional durability. These findings have the potential to pave a promising path for the advancement of high-density nonvolatile memory devices.

2. Experimental

The reagents utilized throughout the experiment comprised zinc acetate dihydrate ($Zn(C_2H_3O_2)\cdot 2H_2O$, 99%), ethanolamine ($NH_2(CH_2)_2OH$, 99.6%), and 2-Methoxyethanol ($C_3H_8O_2$, 99.5%). All of these reagents were procured from Sigma-Aldrich and used as received. The FTO glass, model KV-FTO-R15T22, was purchased from Zhuhai Kaivo Optoelectronic Technology Co., Ltd. (Zhuhai, China). The conductive oxide layer of this substrate is fabricated through magnetron sputtering, achieving a thickness of ~400 nm and possessing a resistivity of ~15 Ω/square. Before utilization, the FTO glass is cut into small pieces of 1 cm × 2 cm dimensions and thoroughly cleaned through an ultrasonic cleaning process to ensure its surface is pristine and ready for subsequent applications. The W target material for sputtering is purchased from Nanchang Hanchen new material technology Co., Ltd. (Nanchang, China), with a diameter of 2 inches, a thickness of 3 mm, and a purity of 3N5.

As illustrated in Figure 1, the synthesis begins with the preparation of a ZnO precursor solution. This is achieved by dissolving 0.5 mM of $Zn(C_2H_3O_2)\cdot 2H_2O$ in a mixture containing 20 mL of $C_3H_8O_2$ and 600 µL of $NH_2(CH_2)_2OH$. After stirring for 12 h at 60 °C, a yellow and transparent solution is obtained. Subsequently, 100 µL of this ZnO precursor solution is applied to substrates using a spin-coating technique. Initially, the coating is performed at a speed of 1000 rpm for 10 s, followed by an increase to 3500 rpm for 30 s. Once the deposition is complete, the spin-coated sample is gently dried at 60 °C for 5 min. This spin-coating process is repeated five times to ensure the formation of a uniform and dense ZnO precursor film on the FTO substrate. Subsequently, the samples are subjected to heating within a muffle furnace, maintained at 800 °C for 10 min. This step not only evaporates the solution but also removes any organic residues, resulting in the formation of a robust ZnO nanofilm. The principal chemical reactions occur during the heat treatment phase. Initially, $Zn(C_2H_3O_2)\cdot 2H_2O$, upon heating, loses its crystal water and decomposes to produce $Zn(CH_3COO)_2$ and water vapor. Subsequently, the $Zn(CH_3COO)_2$ further decomposes and oxidizes to form ZnO. During this process, $NH_2(CH_2)_2OH$ serves as a stabilizer and undergoes complexation reactions with $Zn(CH_3COO)_2$, influencing its decomposition process. It is noteworthy that $C_3H_8O_2$ primarily functions as a solvent in this system. It assists in dissolving the $Zn(C_2H_3O_2)\cdot 2H_2O$ and $NH_2(CH_2)_2OH$, facilitating the formation of a suitable solution for spin-coating. Finally, the circular W electrodes with a diameter of 100 µm and thickness of 100 nm were deposited directly on the FTO substrate by DC magnetron sputtering and patterned through a metal shadow mask, resulting in a functional and well-structured W/ZnO/FTO memory device.

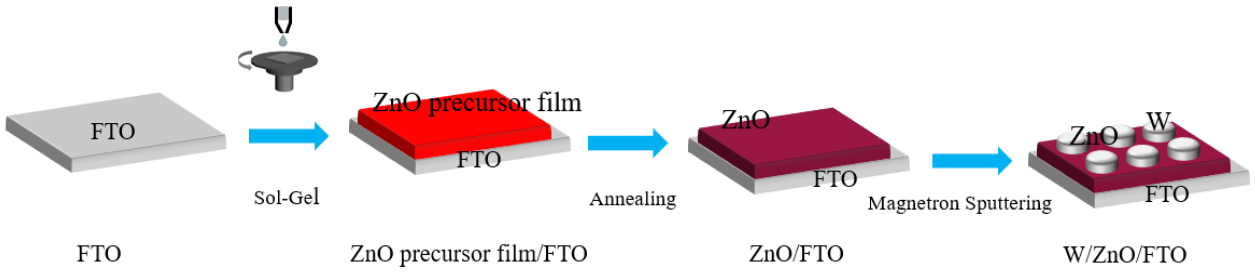

Figure 1. Schematic diagram of the synthesis process for the W/ZnO/FTO memory device.

The morphologies and structures were observed using field-emission scanning electron microscopy (FESEM; FEI Nova NanoSEM 450, Lincoln, NU, USA) and X-ray diffraction (XRD; PANalytical PW3040/60, Cambridge, UK), respectively. During the observation using FESEM, the accelerating voltage was set to 5 KeV, and the working distance was maintained at 10 mm. To verify the chemical states of these samples, X-ray photoelectron

spectroscopy (XPS; AXIS-ULTRA DLD-600W, Shimadzu, Kyoto, Japan) was employed. The absorption of ZnO was characterized using a UV/visible/near-infrared spectrophotometer (Lambda 950, Perkin Elmer, Cambridge, MA, USA). To eliminate any potential interference from the absorption of the FTO substrate on the results, a piece of FTO glass without ZnO film deposition was placed in the reference position during testing. The electronic properties of the memory device were monitored using an Agilent B2901A semiconductor parameter analyzer. All these experimental procedures were conducted under ambient atmospheric conditions.

3. Results and Discussion

Figure 2a depicts a top-view SEM image of the precisely fabricated ZnO thin films. It is evident from the image that the film is composed of uniformly distributed and densely packed ZnO grains. The inset in Figure 2a illustrates the grain size distribution of ZnO, revealing that the majority of grain sizes fall within the range of 25–50 nm, with an average grain size of approximately 40 nm. Figure 2b presents a cross-sectional SEM image of the ZnO film. As can be observed, the ZnO film exhibits a tight adhesion to the FTO substrate, indicating no sign of delamination. To enhance the distinction, an orange dashed line has been added at the interface between the two materials. In the horizontal direction, the ZnO film appears continuous and compact, with no apparent gaps or pores. Furthermore, the thickness of the ZnO film is relatively uniform, with an average thickness of approximately 450 nm.

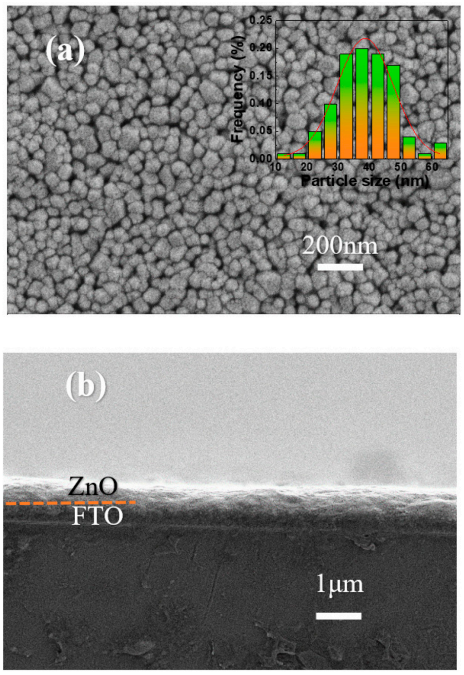

Figure 2. (**a**) Top-view and (**b**) cross-sectional SEM images of the as prepared ZnO thin films. The inset shows the histogram of the size distribution of the grain diameters.

Figure 3 presents the XRD pattern of the ZnO/FTO sample. To provide a clearer characterization of the crystal structure of ZnO, an XRD pattern of the FTO substrate without ZnO is included as a comparative reference. As shown in Figure 3, the (002) diffraction peak is significantly prominent in the XRD pattern, while peaks corresponding to (101), (102), (110), (103), and (112) diffraction are absent, indicating that the as prepared ZnO thin films match with the hexagonal wurtzite phase (JCPDS Card No. 36-1451) [5]. This suggests that the ZnO thin films exhibit a preferential growth orientation along the

(002) plane. The average crystalline size D of the as prepared ZnO nanograins can be obtained by Scherer's equation as

$$D = \frac{0.9\lambda}{\beta cos\theta} \quad (1)$$

where β is fullwidth at half-maxima, λ is the X-ray wavelength (1.5406 Å), and θ is the diffraction angle. The average crystalline size of the as prepared ZnO nanograins is found to be about 37 nm. This closely aligns with the SEM results presented in Figure 2, demonstrating the intrinsic property of the as-prepared ZnO thin films.

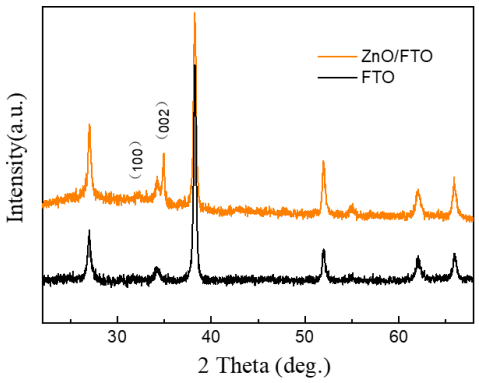

Figure 3. XRD pattern of the FTO substrate and as-prepared ZnO thin films.

To further establish the chemical states of the ZnO thin films under investigation, XPS measurements were conducted. Figure 4a exhibits the overall XPS spectra, revealing the presence of Zn, O, and C elements within the prepared ZnO thin films. Notably, the C element typically originates from atmospheric carbon adsorbed on the surface of the thin films, serving as a reference for calibrating the Zn and O elements. Figure 4b displays the high-resolution XPS spectrum of Zn 2p along with the corresponding Gaussian fitted peaks. Distinctly, the Zn 2p XPS peaks are observable at binding energies close to 1044.14 eV and 1021.09 eV. Furthermore, the calculated spin-orbit splitting binding energy between the Zn $2p^{3/2}$ and Zn $2p^{1/2}$ states is approximately 23.05 eV, indicating the presence of Zn^{2+} ions in the synthesized ZnO thin films [5,21]. As shown in Figure 4c, the asymmetric O 1s XPS spectrum can be deconvoluted into three distinct Gaussian fitting peaks centered at binding energies of 529.88 eV, 531.36 eV, and 532.39 eV, respectively. Importantly, the relative concentration of lattice oxygen, determined from the peak area at 529.88 eV, is found to be 59.5%, which surpasses the concentration of oxygen vacancies (40.3%) at 531.36 eV. Additionally, the atomic percentage of the Zn element is approximately 29.9%, whereas the atomic percentage of lattice oxygen is estimated to be about 23.5% in the ZnO thin films. Consequently, the XPS spectrum analysis reveals the existence of oxygen vacancies, which serve as trapping centers and contribute to the nonvolatile resistive switching behavior of the device.

Figure 5a,b illustrate the absorption spectra and the corresponding Tauc plot, respectively. To eliminate the influence of the FTO substrate on the results, during testing, the ZnO/FTO sample was placed at the test position, and a FTO substrate without ZnO was placed at the comparison position. Specifically, the absorption of the ZnO film was obtained by subtracting the absorption of the FTO substrate from the absorption of the ZnO/FTO sample. Evidently, these ZnO thin films, consisting of nanograins, exhibit remarkable absorptivity, with an absorption edge situated approximately at 308 nm. Their energy band gap E_g can be accurately assessed using the Tauc relation [42]:

$$(\alpha hv)^n = A(hv - E_g) \quad (2)$$

where α, h, v, and A are the absorbance coefficient, Planck's constant, vibration frequency, and the optical constant of the ZnO thin films, respectively. The value of the exponent

n is dependent on the type of material and the transition mechanism at play. Since the ZnO thin films that have been fabricated are direct bandgap materials, the value of n is consequently set to 2. As depicted in Figure 5b, the calculated E_g is approximately 4.1 eV. This value is higher than that reported for pristine ZnO bulk material (3.37 eV) [21], further underscoring the unique intrinsic properties of our prepared ZnO thin films due to their nanoscale dimensions.

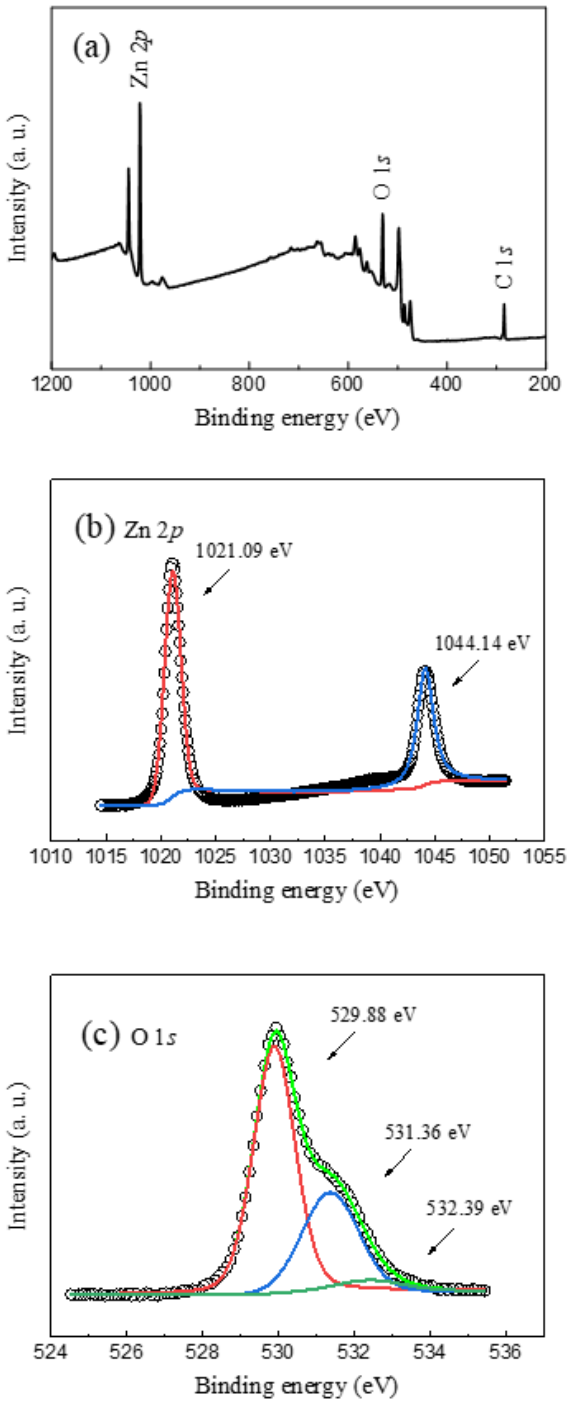

Figure 4. XPS spectra of the ZnO thin films: (**a**) the XPS survey spectra, the high resolution XPS spectra of the (**b**) Zn 2*p*, and (**c**) O 1*s*, respectively.

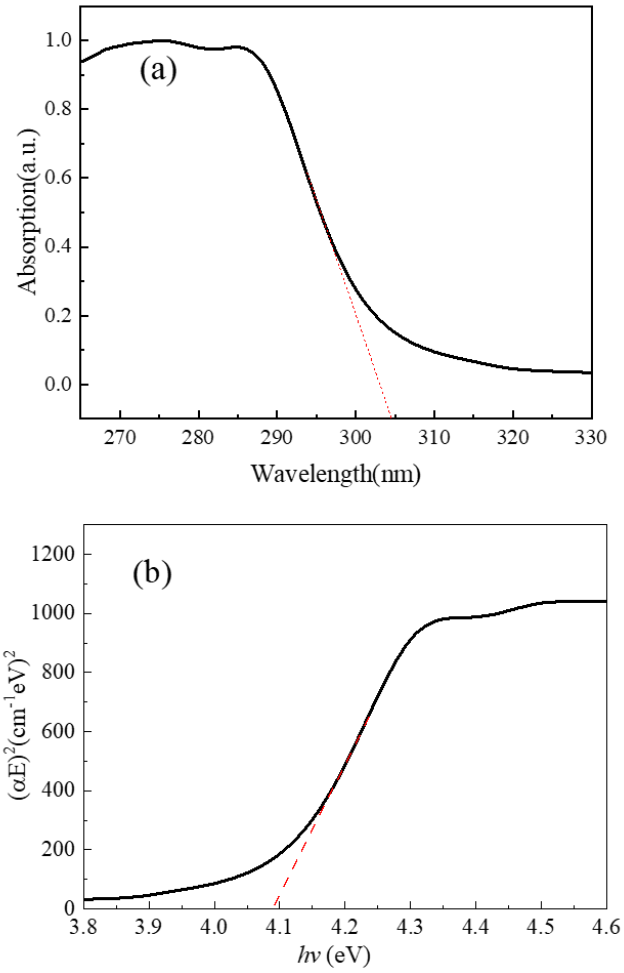

Figure 5. Optical characteristics of the ZnO thin films. (**a**) Photoabsorbance response of the ZnO thin films, (**b**) Tauc plot of the optical band gap for the ZnO thin films.

To assess the nonvolatile resistive switching properties exhibited by such a W/ZnO/FTO memory device, a thorough analysis of its I–V characteristics was conducted. Figure 6a,b depict the I-V curves of the devices plotted in the linear and semi-logarithmic scales under the voltage sweep of 0 V $\rightarrow$ +2.5 V $\rightarrow$ 0 V $\rightarrow$ −3.5 V $\rightarrow$ 0 V for the consecutive 600 resistive switching cycles, respectively. In its initial state, the device exhibits an HRS. Upon exposure to a forward scanning voltage of +2.5 V, the device undergoes a transition from the HRS to an LRS, which corresponds to the set process. Subsequently, the device remains in this LRS until a negative scanning voltage ranging from 0 V to −3.5 V is applied, whereupon it reverts to the HRS, marking the reset process. Notably, the set process of the W/ZnO/FTO memory device is triggered by a forward scanning voltage, while the reset process is completed at a negative scanning voltage. Furthermore, the device maintains its state consistently even after consecutive 600 resistive switching cycles, operated under identical preconditions. The absence of any abrupt changes in current, coupled with repeated erasure consistency, indicates the repeatability, stability, and nonvolatility of the device. Additionally, the I-V curve exhibits asymmetry in the LRS, suggestive of its self-rectifying characteristics. This feature further enhances the versatility and reliability of the device for various memory applications.

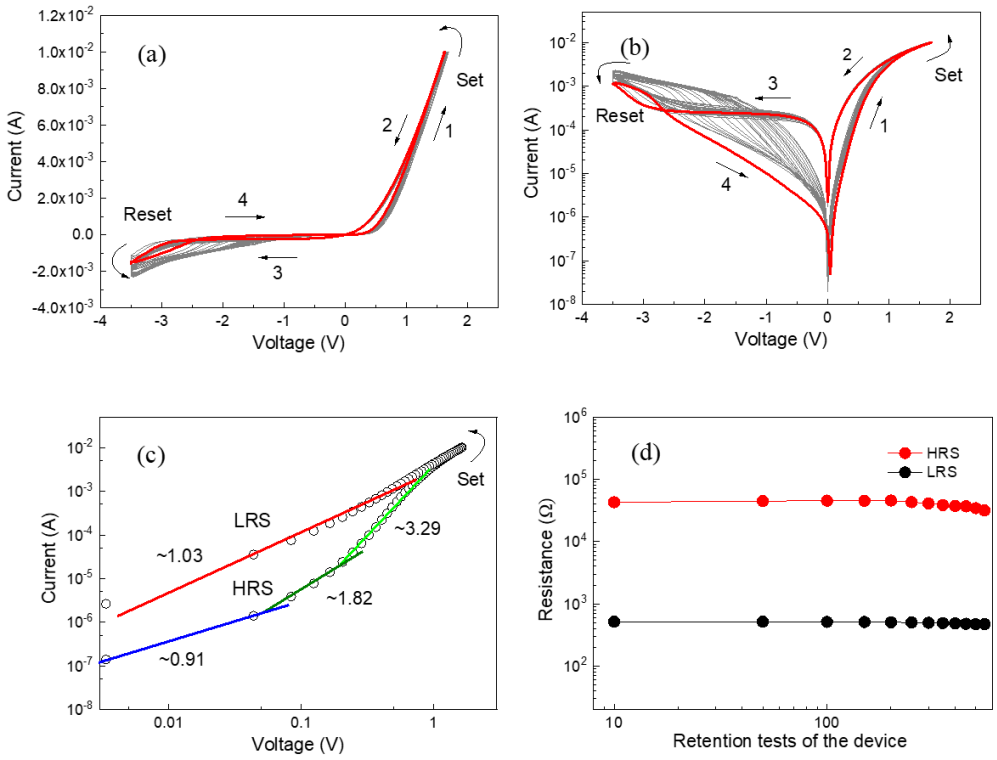

Figure 6. (**a**) The *I-V* response of the W/ZnO/FTO memory device plotted in the linear scale during the consecutive 600 resistive switching cycles, (**b**) The *I-V* plot of the W/ZnO/FTO memory device plotted in the semi-logarithmic scale, (**c**) The double-logarithmic *I-V* plot of the W/ZnO/FTO memory device. (**d**) The retention tests of the W/ZnO/FTO memory device at the reading voltage of 0.1 V.

During the LRS, the I–V curve exhibits linearity with a slope approximating 1.03, as depicted in Figure 6c. This linearity aligns with ohmic conduction, which is attributed to the thermally excited electrons within the system [6,9,10,13]. Furthermore, in the HRS, the I–V curve can be categorized into three distinct sections, each with slopes of approximately 0.91, 1.82, and 3.29, respectively. These slopes are indicative of the typical trap-controlled space charge-limited conduction (SCLC) mechanism operating within the device during the HRS [4]. According to the conducting filament model applicable to the LRS, the device's current flows through conducting filaments comprised of intrinsic oxygen vacancies. Consequently, this arrangement gives rise to the observed ohmic conduction behavior. In the reset process, the oxygen vacancies migrate towards the top electrode and recombine with oxygen ions situated nearby. This recombination process leads to the partial rupture of the conductive nanofilaments, effectively switching the device from the LRS back to its intrinsic HRS.

Figure 6d illustrates the retention tests conducted on the W/ZnO/FTO memory device throughout consecutive 600 resistive switching cycles, with a constant reading voltage of 0.1 V. Notably, the resistance ratio of R_{HRS}/R_{LRS} remains consistently maintained, exceeding two orders of magnitude, even at the reading voltage of 0.1 V. This underscores the exceptional reproducibility and reliability of the as-prepared memory device. Table 1 summarizes the performance of the ZnO-based nonvolatile memory devices. It is evident that most current ZnO-based nonvolatile memory devices are fabricated using vapor deposition techniques, such as magnetron sputtering, pulsed laser deposition, and chemical vapor deposition. Among these, magnetron sputtering is the most commonly employed method. While these techniques exhibit promising overall performance, they are associated with two primary issues: (1) The equipment required for these methods is costly, and furthermore, the devices predominantly utilize expensive metals like Au, Pt, and Ag as electrodes, further escalating the production costs. (2) They tend to exhibit a relatively

low resistance ratio, with the majority of devices achieving only around 10 for R_{HRS}/R_{LRS}. In contrast, the solution-based approach utilized in this study significantly simplifies the production process and employs W as a more cost-effective electrode material, making it a more economically viable option. In terms of performance, the proposed method exhibits comparable retention properties to those reported in previous studies, while achieving a higher R_{HRS}/R_{LRS} ratio.

Table 1. Comparison of performance parameters for the ZnO based nonvolatile memory devices.

Structure	V_{set}/V_{reset} (V)	Preparation Process	R_{HRS}/R_{LRS}	Retention	Reference
top-probe/α-Fe_2O_3/ZnO/bottom-probe	−0.55/−	Spin-coating technique	~20	10^3 s	[5]
Al/Si/Al_2O_3/ZnO/Al_2O_3/Al	+7/−7	Pulsed laser deposition	~10	10^3 s	[34]
Cr/ZnO/Pt–Fe_2O_3 NPs/ZnO/Cr	−7/+7	Dip-coating method	~5	10^4 s	[54]
Ag/$BaTiO_3$/γ-Fe_2O_3/ZnO/Ag	+3.1/−4.7	Co-precipitation method	~10	-	[51]
Pt/ZnO/Zn	−4/+5	Hydrothermal method	~10	10 s	[32]
Ag/ZnO/Pt	+1/−1	Magnetron sputtering	~10	10^3 s	[21]
Ag/ZnO/Ag	~+1.6/~−2	Spin-coating technique	<10	3.1×10^3	[46]
Au/ZnO nanorods/AZO	−6/+7	Dip-coating method	~10	-	[38]
Pt/ZnO nanowire/Pt	+0.5/−	Chemical vapor deposition	~1.5	0.9×10^2 s	[50]
Pt/ZnO thin film/Pt	~−1.75/~+2	Magnetron sputtering	~10	10^3 s	[52]
Pt/ZnO/Pt	+1.2/−1	Chemical vapor deposition	~7	10^4 s	[27]
Pt/ZnO/TiN	~+1.25/~−1	Pulsed laser deposition	~2	-	[36]
Ti/ZnO/Pt	~+2/~−1.5	Magnetron sputtering	~10	10^5 s	[49]
Pt/ZnO NRL/ITO	+0.72/−0.59	Hydrothermal method	~10	10^3 s	[48]
Cu/ZnO/ITO	+1/−1.7	Magnetron sputtering	~10	-	[44]
ITO/HfO_x/ZnO/ITO	~−3/~+3	Magnetron sputtering	~10	10^4 s	[43]
Au/ZnO/ITO	~+2.2/~−3.8	Magnetron sputtering	>10	-	[53]
Pt/ZnO/ITO	+1/−1	Cyclic voltammetry deposition	~50	3×10^2 s	[40]
Ag/SA+ZnO NPs/ITO	+2.5/−2.5	Spin-coating technology	~30	10^3 s	[24]
Ag/PTAA/ZnO/ITO	+3/−2	Magnetron sputtering	~20	2.4×10^3 s	[30]
Al/ZnO/NiO/ITO	+4.4/−6.1	Spin-coating technology	~10^4	-	[64]
Al/Ga-doped ZnO/FTO	+2/−2	Hydrothermal method	~1.48	10^3 s	[65]
W/ZnO/FTO	~+0.5/~−1	Spin-coating technique	>10^2	>10^3 s	This work

As previously analyzed, the nonvolatile resistive switching behavior exhibited by the fabricated W/ZnO/FTO memory device, utilizing ZnO thin films, can be attributed to the conducting filament model. This model involves the partial formation and subsequent collapse of conducting nano-filaments, modulated by the inherent oxygen vacancies present within the ZnO thin films. As shown in Figure 7, during the set process, a positive sweeping voltage is applied to the memory device. This voltage drives the oxygen vacancies to migrate and accumulate, moving from the bottom towards the top electrode. Once the applied voltage exceeds the threshold V_{set} (about +0.5 V), the conducting nanofilaments, modulated by the oxygen vacancies, establish a short circuit between the electrodes. Consequently, the device transitions from the HRS to the LRS, marked by a significant surge in current. Following this, the device maintains its LRS until a sufficiently large negative sweeping voltage, V_{reset} (about −1 V), is applied. In the reset process, as the negative sweeping voltage is applied, the oxygen vacancies migrate towards the top W electrode and recombine with oxygen ions in proximity. Simultaneously, the device transitions back to its original HRS, accompanied by a sudden decrease in current at V_{reset}, signifying the occurrence of the reset process. Hence, the partial formation and collapse of conducting nanofilaments, modulated by the inherent oxygen vacancies, are postulated to underlie the nonvolatile resistive switching behavior observed in the W/ZnO/FTO memory device.

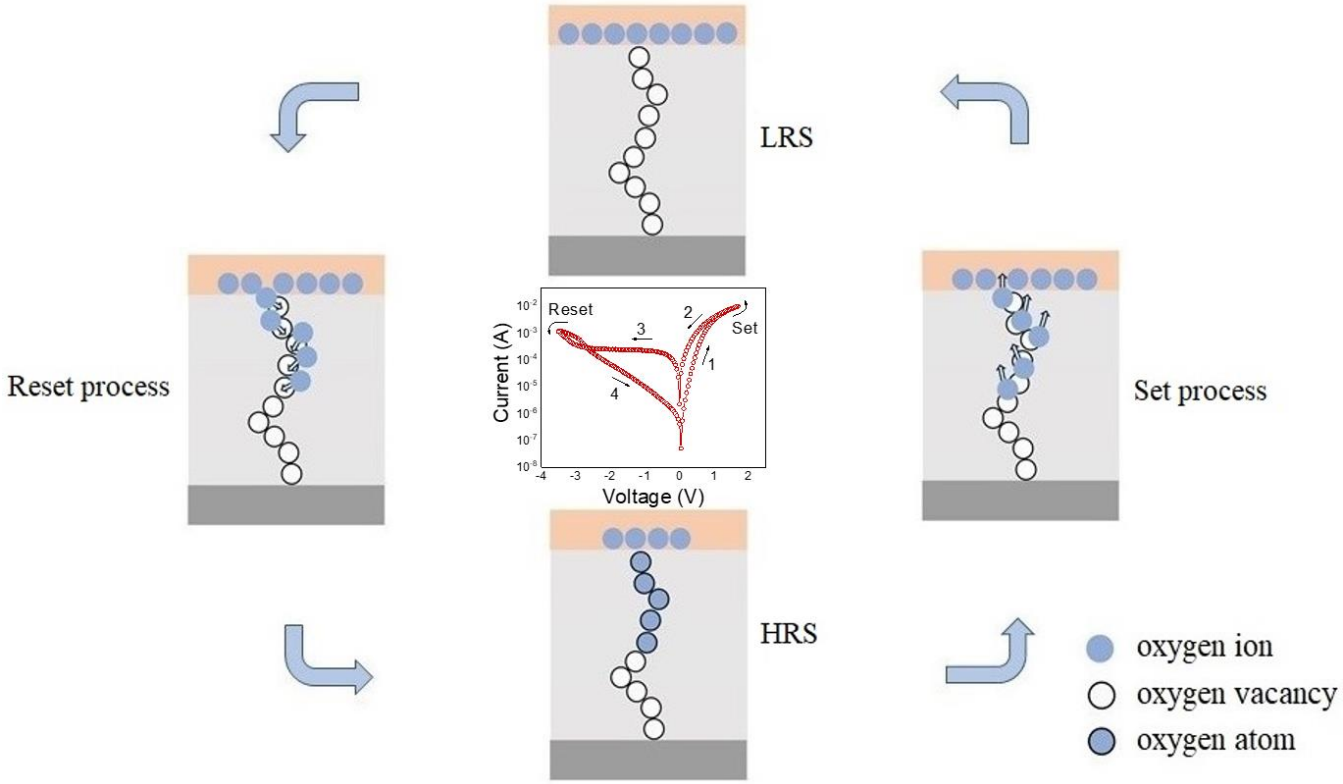

Figure 7. Filamentary resistive switching mechanism of the W/ZnO/FTO memory device.

4. Conclusions

In summary, ZnO thin films with preferential (002) plane growth orientation were successfully fabricated on FTO substrates via a facile sol-gel spin-coating method. The resistive switching properties of the resulting W/ZnO/FTO memory device, utilizing these thin films, were thoroughly investigated. The device exhibited remarkable nonvolatile and bipolar resistive switching characteristics, including a high resistance ratio exceeding two orders of magnitude at 0.1 V, robust resistance retention (up to 10^3 s), ultra-low set (+0.5 V) and reset (−1 V) voltages, and exceptional durability. The carrier transport in the device can be attributed to ohmic conduction in the LRS and trap-controlled SCLC in

the HRS. Additionally, the formation and rupture of conducting filaments modulated by intrinsic oxygen vacancies underlie the observed nonvolatile and bipolar resistive switching behaviors. Compared with previously reported ZnO-based nonvolatile memory devices, the solution-based process adopted in this paper is simpler and the raw materials are cheaper, achieving equivalent or better performance, making it more economical. In the future, the scalability, reproducibility, and reliability of such devices should be further improved to achieve better information storage and retrieval.

Author Contributions: Writing—original draft preparation, writing—review and editing, X.S.; Conceptualization, methodology, supervision, Z.Y. All authors have read and agreed to the published version of the manuscript.

Funding: This project is supported by the National Natural Science Foundation of China (Grant Nos. AD19110038, AD21238033), the Guangxi Science and Technology Project (Grant Nos. AD19110038, AD21238033), the Scientific Research Foundation of Guangxi University of Science and Technology (Grant No. 19Z07), the Tianshan Innovation Team Program of Xinjiang Uygur Autonomous Region of China (2023D14001), and the Natural Science Foundation of Xinjiang Uygur Autonomous Region of China (Grant No. 2022D01C20).

Institutional Review Board Statement: Not applicable.

Informed Consent Statement: Not applicable.

Data Availability Statement: Data are contained within the article.

Conflicts of Interest: The authors declare no conflict of interest.

References

1. Chua, L.O. Memristor-The missing circuit element. *IEEE Trans. Circuit Theory* **1971**, *18*, 507–519. [CrossRef]
2. Strukov, D.B.; Snider, G.S.; Stewart, D.R.; Williams, R.S. The missing memristor found. *Nature* **2008**, *453*, 80–83. [CrossRef]
3. Milano, G.; Luebben, M.; Ma, Z.; Dunin-Borkowski, R.; Boarino, L.; Pirri, C.F.; Waser, R.; Ricciardi, C.; Valov, I. Self-limited single nanowire systems combining allin-one memristive and neuromorphic functionalities. *Nat. Commun.* **2018**, *9*, 5151. [CrossRef] [PubMed]
4. Ren, S.X.; Dong, W.C.; Tang, H.; Tang, L.Z.; Li, Z.H.; Sun, Q.; Yang, H.F.; Yang, Z.G.; Zhao, J.J. High-efficiency magnetic modulation in Ti/ZnO/Pt resistive random-access memory devices using amorphous zinc oxide film. *Appl. Surf. Sci.* **2019**, *488*, 92–97. [CrossRef]
5. Sarkar, D.; Singh, A.K. Mechanism of Nonvolatile Resistive Switching in ZnO/α-Fe_2O_3 Core-Shell Heterojunction Nanorod Arrays. *J. Phys. Chem. C* **2017**, *121*, 12953–12958. [CrossRef]
6. Yu, Z.Q.; Jia, J.H.; Qu, X.R.; Wang, Q.C.; Kang, W.B.; Liu, B.S.; Xiao, Q.Q.; Gao, T.H.; Xie, Q. Tunable resistive switching behaviors and mechanism of the W/ZnO/ITO memory cell. *Molecules* **2023**, *28*, 5313. [CrossRef]
7. Qi, M.; Zhang, X.; Yang, L.; Wang, Z.Q.; Xu, H.Y.; Liu, W.Z.; Zhao, X.N.; Liu, Y.C. Intensity-modulated LED achieved through integrating p-GaN/n-ZnO heterojunction with multilevel RRAM. *Appl. Phys. Lett.* **2018**, *113*, 223503. [CrossRef]
8. Chen, J.; Wu, Y.L.; Zhu, K.L.; Sun, F.; Guo, C.G.; Wu, X.L.; Cheng, G.A.; Zheng, R.T. Core-shell copper nanowire-TiO_2 nanotube arrays with excellent bipolar resistive switching properties. *Electrochim. Acta* **2019**, *316*, 133–142. [CrossRef]
9. Kyung, M.K.; Byung, J.C.; Yong, C.S.; Seol, C.; Cheol, S.H. Anode-interface localized filamentary mechanism in resistive switching of TiO_2 thin film. *Appl. Phys. Lett.* **2007**, *91*, 012907. [CrossRef]
10. Yu, Z.Q.; Sun, T.Y.; Liu, B.S.; Zhang, L.; Chen, H.J.; Fan, X.S.; Sun, Z.J. Self-rectifying and forming-free nonvolatile memory behavior in single-crystal TiO_2 nanowire memory device. *J. Alloys Compd.* **2021**, *858*, 157749. [CrossRef]
11. Persson, K.M.; Ram, M.S.; Kilpi, O.P.; Borg, M.; Wernersson, L.E. Cross-Point Arrays with Low-Power ITO-HfO_2 Resistive Memory Cells Integrated on Vertical III-V Nanowires. *Adv. Electron. Mater.* **2020**, *6*, 2000154. [CrossRef]
12. Mahmoud, N.A.; Maximilian, S.; Brian, C.O.; Erik, J.L.; Sayed, Y.S.; Marc, T.; Jillian, M.B. Bipolar Resistive Switching in Junctions of Gallium Oxide and p-type Silicon. *Nano Lett.* **2021**, *21*, 2666–2674. [CrossRef]
13. Yu, Z.Q.; Xu, J.M.; Liu, B.S.; Sun, Z.J.; Huang, Q.N.; Ou, M.L.; Wang, Q.C.; Jia, J.H.; Kang, W.B.; Xiao, Q.Q.; et al. A Facile Hydrothermal Synthesis and Resistive Switching Behavior of α-Fe_2O_3 Nanowire Arrays. *Molecules* **2023**, *28*, 3835. [CrossRef] [PubMed]
14. Yao, C.Y.; Li, J.C.; Thatikonda, S.K.; Ke, Y.F.; Qin, N.; Bao, D.H. Introducing a thin MnO_2 layer in Co_3O_4-based memory to enhance resistive switching and magnetization modulation behaviors. *J. Alloys Compd.* **2020**, *823*, 153731. [CrossRef]
15. Huang, C.H.; Matsuzaki, K.; Nomura, K. Threshold switching of non-stoichiometric CuO nanowire for selector application. *Appl. Phys. Lett.* **2020**, *116*, 023503. [CrossRef]
16. Hsu, C.C.; Wang, S.Y.; Lin, Y.S.; Chen, Y.T. Self-rectifying and interface-controlled resistive switching characteristics of molybdenum oxide. *J. Alloys Compd.* **2019**, *779*, 609–617. [CrossRef]

17. You, B.K.; Park, W.I.; Kim, J.M.; Park, K.I.; Seo, H.K.; Lee, J.Y.; Jung, Y.S.; Lee, K.J. Formation in Resistive Memories by Self-Assembled Nanoinsulators Derived from a Block Copolymer. *ACS NANO* **2014**, *9*, 9492–9502. [CrossRef] [PubMed]
18. Huang, C.H.; Chang, W.C.; Huang, J.S.; Lin, S.M.; Chueh, Y.L. Resistive Switching of Sn-doped In_2O_3/HfO_2 core-shell nanowire: Geometry Architecture Engineering for Nonvolatile Memory. *Nanoscale* **2017**, *9*, 6920–6928. [CrossRef] [PubMed]
19. Sun, Y.M.; Song, C.; Yin, J.; Qiao, L.L.; Wang, R.; Wang, Z.Y.; Chen, X.Z.; Yin, S.Q.; Saleem, M.S.; Wu, H.Q.; et al. Modulating metallic conductive filaments via bilayer oxides in resistive switching memory. *Appl. Phys. Lett.* **2019**, *114*, 193502. [CrossRef]
20. Younis, A.; Chu, D.W.; Li, S.A. Stochastic memristive nature in Co-doped CeO_2 nanorod arrays. *Appl. Phys. Lett.* **2013**, *103*, 253504. [CrossRef]
21. Zoolfakar, A.S.; Kadir, R.A.; Rani, R.A.; Balendhran, S.; Liu, X.J.; Kats, E.; Bhargava, S.K.; Bhaskaran, M.; Sriram, S.; Zhuiykov, S.; et al. A comprehensive review of ZnO materials and devices. *Phys. Chem. Chem. Phys.* **2013**, *15*, 10376. [CrossRef]
22. Park, J.; Biju, K.P.; Jung, S.; Lee, W.; Lee, J.; Kim, S.; Park, S.; Shin, J.; Hwang, H. Multibit Operation of TiO_x-Based ReRAM by Schottky Barrier Height Engineering. *IEEE Electron Device Lett.* **2011**, *32*, 476–478. [CrossRef]
23. Liang, K.; Huang, C.; Lai, C.; Huang, J.; Tsai, H.; Wang, Y.; Shih, Y.; Chang, M.; Lo, S.; Chueh, Y. Single CuO_x Nanowire Memristor: Forming-Free Resistive Switching Behavior. *ACS Appl. Mater. Interfaces* **2014**, *6*, 16537–16544. [CrossRef]
24. Wang, F.J.; Chen, K.J.; Yi, X.R.; Lin, Y.N.; Zhuang, S.L. A study on sodium alginate based memristor: From typical to self-rectifying. *Mater. Lett.* **2023**, *338*, 134037. [CrossRef]
25. Miccoli, I.; Spampinato, R.; Marzo, F.; Prete, P.; Lovergine, N. DC-magnetron sputtering of ZnO:Al films on (00.1)Al_2O_3 substrates from slip-casting sintered ceramic targets. *Appl. Surf. Sci.* **2014**, *313*, 418–423. [CrossRef]
26. Lehraki, N.; Aida, M.S.; Abed, S.; Attaf, N.; Attaf, A.; Poulain, M. ZnO thin films deposition by spray pyrolysis: Influence of precursor solution properties. *Curr. Appl. Phys.* **2012**, *12*, 1283–1287. [CrossRef]
27. Milano, G.; Porro, S.; Ali, M.Y.; Bejtka, K.; Bianco, S.; Beccaria, F.; Chiolerio, A.; Pirri, C.F.; Ricciardi, C. Unravelling Resistive Switching Mechanism in ZnO NW Arrays: The Role of the Polycrystalline Base Layer. *J. Phys. Chem. C* **2018**, *12*, 866–874. [CrossRef]
28. Garratt, E.; Prete, P.; Lovergine, N.; Nikoobakht, B. Observation and Impact of a "Surface Skin Effect" on Lateral Growth of Nanocrystals. *J. Phys. Chem. C* **2017**, *121*, 14845–14853. [CrossRef]
29. Zhang, J.; Yang, H.; Zhang, Q.L.; Dong, S.R.; Luo, J.K. Bipolar resistive switching characteristics of low temperature grown ZnO thin films by plasma-enhanced atomic layer deposition. *Appl. Phys. Lett.* **2013**, *102*, 012113. [CrossRef]
30. Khan, S.A.; Rahmani, M.K.; Khan, W.U.; Kim, J.; Bae, J.; Kang, M.H. Multistate Resistive Switching with Self-Rectifying Behavior and Synaptic Characteristics in a Solution-processed ZnO/PTAA Bilayer Memristor. *J. Electrochem. Soc.* **2022**, *169*, 063517. [CrossRef]
31. Sokolov, A.S.; Jeon, Y.R.; Kim, S.; Ku, B.; Choi, C. Bio-realistic synaptic characteristics in the cone-shaped ZnO memristive device. *NPG Asia Mater.* **2019**, *11*, 5. [CrossRef]
32. Quintana, A.; Gómez, A.; Baró, M.D.; Suriñach, S.; Pellicer, E.; Sort, J. Self-templating faceted and spongy single-crystal ZnO nanorods: Resistive switching and enhanced piezoresponse. *Mater. Des.* **2017**, *133*, 54–61. [CrossRef]
33. Reddy, I.N.; Reddy, C.V.; Sreedhar, M.; Cho, M.; Shim, J.; Reddy, V.R.; Choi, C.-J.; Kim, D. Effect of seed layers (Al, Ti) on optical and morphology of Fe-doped ZnO thin film nanowires grown on Si substrate via electron beam evaporation. *Mater. Sci. Semicond. Process.* **2017**, *71*, 296–303. [CrossRef]
34. Sekhar, K.C.; Kamakshi, K.; Bernstorff, S.; Gomes, M.J.M. Effect of annealing temperature on photoluminescence and resistive switching characteristics of ZnO/Al_2O_3 multilayer nanostructures. *J. Alloys Compd.* **2015**, *619*, 248–252. [CrossRef]
35. Zhou, Z.; Xiu, F.; Jiang, T.F.; Xu, J.G.; Chen, J.; Liu, J.Q.; Huang, W. Solution-processable zinc oxide nanorods and a reduced graphene oxide hybrid nanostructure for highly flexible and stable memristor. *J. Mater. Chem. C* **2019**, *7*, 10764–10768. [CrossRef]
36. Punugupati, S.; Temizer, N.K.; Narayan, J.; Hunte, F. Structural and resistance switching properties of epitaxial Pt/ZnO/TiN/Si(001) heterostructures. *J. Appl. Phys.* **2014**, *115*, 234501. [CrossRef]
37. Manna, A.K.; Dash, P.; Das, D.; Srivastava, S.K.; Sahoo, P.K.; Kanjilal, A.; Kanjilal, D.; Varma, S. Resistive switching properties and photoabsorption behavior of Ti ion implanted ZnO thin films. *Ceram. Int.* **2022**, *48*, 3303–3310. [CrossRef]
38. Sun, Y.H.; Yan, X.Q.; Zheng XLiu, Y.H.; Zhao, Y.G.; Shen, Y.W.; Liao, Q.L.; Zhang, Y. High On-Off Ratio Improvement of ZnO-Based Forming-Free Memristor by Surface Hydrogen Annealing. *ACS Appl. Mater. Interfaces* **2015**, *7*, 7382–7388. [CrossRef]
39. Xu, Z.D.; Yu, L.N.; Xu, X.G.; Miao, J.; Jiang, Y. Effect of oxide/oxide interface on polarity dependent resistive switching behavior in ZnO/ZrO_2 heterostructures. *Appl. Phys. Lett.* **2014**, *104*, 192903. [CrossRef]
40. Huang, J.S.; Lee, C.Y.; Chin, T.S. Forming-free bipolar memristive switching of ZnO films deposited by cyclic-voltammetry. *Electrochim. Acta* **2013**, *91*, 62–68. [CrossRef]
41. Park, J.J.; Lee, S.H.; Lee, J.H.; Yong, K.J. A Light Incident Angle Switchable ZnO Nanorod Memristor: Reversible Switching Behavior Between Two Non-Volatile Memory Devices. *Adv. Mater.* **2013**, *25*, 6423–6429. [CrossRef]
42. Shen, X.; Lin, X.; Peng, Y.; Zhang, Y.; Long, F.; Han, Q.; Wang, Y.; Han, L. Two-Dimensional Materials for Highly Efficient and Stable Perovskite Solar Cells. *Nano-Micro Lett.* **2024**, *16*, 201. [CrossRef]
43. Wu, S.J.; Wang, F.; Zhang, Z.C.; Li, Y.; Han, Y.M.; Yang, Z.C.; Zhao, J.S.; Zhang, K.L. High uniformity and forming-free ZnO-based transparent RRAM with HfO_x inserting layer. *Chin. Phys. B* **2018**, *27*, 087701. [CrossRef]
44. Simanjuntak, F.M.; Ohno, T.; Samukawa, S.J. Neutral Oxygen Beam Treated ZnO-Based Resistive Switching Memory Device. *ACS Appl. Electron. Mater.* **2019**, *1*, 18–24. [CrossRef]

45. Jung, J.; Kwon, D.; Jung, H.; Lee, K.; Yoon, T.; Kang, C.J.; Lee, H.H. Multistate resistive switching characteristics of ZnO nanoparticles embedded polyvinylphenol device. *J. Ind. Eng. Chem.* **2018**, *64*, 85–89. [CrossRef]
46. Choi, K.H.; Mustafa, M.; Rahman, K.; Jeong, B.K.; Doh, Y.H. Cost-effective fabrication of memristive devices with ZnO thin film using printed electronics technologies. *Appl. Phys. A* **2012**, *106*, 165–170. [CrossRef]
47. Patil, S.R.; Chougale, M.Y.; Rane, T.D.; Khot, S.S.; Patil, A.A.; Bagal, O.S.; Jadhav, S.D.; Sheikh, A.D.; Kim, S.; Dongale, T.D. Solution-Processable ZnO Thin Film Memristive Device for Resistive Random Access Memory Application. *Electronics* **2018**, *7*, 445. [CrossRef]
48. Chang, W.Y.; Lin, C.; He, J.; Wu, T. Resistive switching behaviors of ZnO nanorod layers. *Appl. Phys. Lett.* **2012**, *96*, 242109. [CrossRef]
49. Wang, J.R.; Pan, R.B.; Cao, H.T.; Wang, Y.; Liang, L.Y.; Zhang, H.L.; Gao, J.H.; Zhuge, F. Anomalous rectification in a purely electronic memristor. *Appl. Phys. Lett.* **2016**, *109*, 143505. [CrossRef]
50. Karthik, K.R.G.; Prabhakar, R.R.; Hai-, L.; Batabyal, S.K.; Huang, Y.Z.; Mhaisalkar, S.G. A ZnO nanowire resistive switch. *Appl. Phys. Lett.* **2013**, *103*, 123114. [CrossRef]
51. Sun, B.; Liu, Y.H.; Zhao, W.X.; Chen, P. Magnetic-field and white-light controlled resistive switching behaviors in Ag/$BiFeO_3$/γ-Fe_2O_3/FTO device. *RSC Adv.* **2015**, *5*, 13513–13518. [CrossRef]
52. Huang, C.; Huang, J.; Lai, C.; Huang, H.; Lin, S.; Chueh, Y. Manipulated Transformation of Filamentary and Homogeneous Resistive Switching on ZnO Thin Film Memristor with Controllable Multistate. *ACS Appl. Mater. Interfaces* **2013**, *5*, 6017–6023. [CrossRef]
53. Wang, H.J.; Zhu, Y.Y.; Liu, Y. Characteristics of the bipolar resistive switching behavior in memory device with Au/ZnO/ITO structure. *Chin. J. Phys.* **2018**, *56*, 3073–3077. [CrossRef]
54. Yoo, E.J.; Kang, S.Y.; Shim, E.L.; Yoon, T.S.; Kang, C.J.; Choi, Y.J. Influence of Incorporated Pt-Fe_2O_3 Core-Shell Nanoparticles on the Resistive Switching Characteristics of ZnO Thin Film. *J. Nanosci. Nanotechnol.* **2015**, *15*, 8622–8626. [CrossRef]
55. Huang, C.; Huang, J.; Lin, S.; Chang, W.; He, J.; Chueh, Y. ZnO_{1-x} Nanorod Arrays/ZnO Thin Film Bilayer Structure: From Homojunction Diode and High-Performance Memristor to Complementary 1D1R Application. *ACS Nano* **2012**, *6*, 8407–8414. [CrossRef]
56. Yu, Z.Q.; Han, X.; Xu, J.M.; Chen, C.; Qu, X.R.; Liu, B.S.; Sun, Z.J.; Sun, T.Y. The Effect of Nitrogen Annealing on the Resistive Switching Characteristics of the W/TiO_2/FTO Memory Device. *Sensors* **2023**, *23*, 3480. [CrossRef]
57. Sun, T.Y.; Liu, Y.; Tu, J.; Zhou, Z.P.; Cao, L.; Liu, X.P.; Li, H.O.; Li, Q.; Fu, T.; Zhang, F.B.; et al. Wafer-scale high anti-reflective nano/micro hybrid interface structures via aluminum grain dependent self-organization. *Mater. Des.* **2020**, *194*, 108960. [CrossRef]
58. Yu, Z.Q.; Qu, X.P.; Yang, W.P.; Peng, J.; Xu, Z.M. A facile hydrothermal synthesis and memristive switching performance of rutile TiO_2 nanowire arrays. *J. Alloys Compd.* **2016**, *688*, 37–43. [CrossRef]
59. Yu, Z.Q.; Qu, X.P.; Yang, W.P.; Peng, J.; Xu, Z.M. Hydrothermal synthesis and memristive switching behaviors of single-crystalline anatase TiO_2 nanowire arrays. *J. Alloys Compd.* **2016**, *688*, 294–300. [CrossRef]
60. Yu, Z.Q.; Liu, M.L.; Lang, J.X.; Qian, K.; Zhang, C.H. Resistive switching characteristics and resistive switching mechanism of Au/TiO_2/FTO memristor. *Acta Phys. Sin.* **2018**, *67*, 157302. [CrossRef]
61. Chauhan AK, S.; Sharma, D.K.; Datta, A. Rate limited filament formation in Al-ZnO-Al bipolar ReRAM cells and its impact on early current window closure during cycling. *J. Appl. Phys.* **2019**, *125*, 104503. [CrossRef]
62. Sun, T.Y.; Yu, F.T.; Tang, X.S.; Li, H.O.; Zhang, F.B.; Xu, Z.M.; Liao, Q.; Yu, Z.Q.; Liu, X.P.; Wangyang, P.H.; et al. Organic-2D composite material-based RRAM with high reliability for mimicking synaptic behavior. *J. Mater.* **2024**, *10*, 440–447. [CrossRef]
63. Solanki, V.; Joshi, S.R.; Mishra, I.; Kabiraj, D.; Mishra, N.C.; Avasthi, D.K.; Varma, S. Oxygen vacancy mediated enhanced photo-absorption from ZnO (0001) nanostructures fabricated by atom beam sputtering. *J. Appl. Phys.* **2016**, *120*, 054303. [CrossRef]
64. Lu, H.P.; Yuan, X.C.; Chen, B.L.; Gong, C.H.; Zeng, H.Z.; Wei, X.H. Self-rectifying resistive switching device based on n-ZnO/p-NiO junction. *J. Sol.-Gel Sci. Technol.* **2017**, *82*, 627–634. [CrossRef]
65. More, S.S.; Patil, P.A.; Kadam, K.D.; Patil, H.S.; Patil, S.L.; Kamat, R.K.; Kim, S.; Dongale, T.D. Resistive switching and synaptic properties modifications in gallium-doped zinc oxide memristive devices. *Results Phys.* **2019**, *12*, 1946–1955. [CrossRef]

Disclaimer/Publisher's Note: The statements, opinions and data contained in all publications are solely those of the individual author(s) and contributor(s) and not of MDPI and/or the editor(s). MDPI and/or the editor(s) disclaim responsibility for any injury to people or property resulting from any ideas, methods, instructions or products referred to in the content.